NANO LETTERS

pubs.acs.org/NanoLett Letter

Wearable Multimodal Sensing System for Synchronously Health−Environmental Monitoring via Hybrid Neuroevolutionary Signal Decoupling

Qisong Jia, Wenhao Ye, Chang Zhang, Zhuoyi Jia, Ji Liu, Tongchao Wang, Liupeng Zhao, Yongshun Liu,* Chen Wang,* Peng Sun,* Zhiyong Fan, and Geyu Lu

Cite This: https://doi.org/10.1021/acs.nanolett.5c01881 Read Online

ACCESS | Metrics & More | Article Recommendations | Supporting Information

ABSTRACT: Wearable sensors are advancing personalized healthcare and environmental safety, yet integrating multimodal sensing remains challenging due to material incompatibility, cross-sensitivity, and environmental interference. To address this gap, we present a monolithic wristband-integrated multimodal sensing platform for simultaneous environmental and physiological monitoring. The system integrates sensors for NO_2, UV irradiance, epidermal temperature, and human pulse signals. A TiO_2/WS_2 heterojunction-based resistive transduction matrix, as the core sensing material, achieves room-temperature NO_2 detection (theoretical limit of detection of 14.4 ppb) with 12-month stability, UV intensity measurement (0.024−1.68 mW/cm^2), epidermal temperature monitoring (25−50 °C, sensitivity of 0.22%/°C), and arterial pulse waveform analysis (P−T−D peak resolution). A hybrid neuroevolutionary algorithm (GA-BP) decouples photo-gas interference, reducing quantification errors to <3.5%. Flexible electronics and selective encapsulation (PDMS, PET shielding) ensure mechanical durability and accurate signal acquisition. The platform demonstrates multifunctional capabilities that enable point-of-care health and environmental monitoring, bridging personalized diagnostics with exposure assessment.

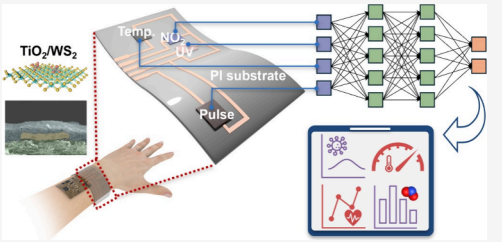

KEYWORDS: *TiO_2/WS_2 heterojunction, multimodal sensing system, wearable electronics, signal decoupling, GA-BP neural network*

Wearable sensors have emerged as pivotal tools for real-time physiological data acquisition, advancing applications in personalized healthcare and clinical diagnostics.[1−4] State-of-the-art systems encompass diverse modalities: electrochemical sweat sensors for metabolite profiling (e.g., glucos and lactate), piezoresistive pulse sensors for cardiovascular monitoring,[5] and thermistors for core body-temperature tracking. Recent advancements extend their utility to environmental safety, particularly for ultraviolet (UV) radiation and hazardous gas detection. Chronic UV exposure is a well-documented etiological factor in dermatological pathologies, including actinic keratosis, basal cell carcinoma, and melanoma.[6,7] Concurrently, nitrogen dioxide (NO_2), a by-product of vehicular emissions, exacerbates respiratory morbidity through oxidative stress and airway inflammation, contributing to conditions such as chronic obstructive pulmonary disease.[8−12]

The integration of multimodal sensing capabilities into unified wearable platforms represents a critical frontier, yet significant challenges persist.[13,14] Conventional fabrication methods—such as screen printing, inkjet patterning,[15,16] and drop casting—suffer from material heterogeneity and structural incompatibility, undermining device reproducibility. These limitations necessitate the development of homogeneous sensing materials capable of transducing multiple stimuli while maintaining consistent performance metrics.[6−17] A unified sensor architecture is equally critical to streamline manufacturing and enhance scalability.[18] A persistent challenge lies in mitigating cross-sensitivity and environmental interference, particularly for room-temperature gas sensors susceptible to UV irradiation and humidity.[14] Additional confounding factors include baseline drift and mechanical deformation artifacts induced by substrate flexure.[8−19] Addressing these issues requires synergistic strategies: (1) tailored encapsulation to isolate sensing elements from external perturbations and (2) advanced signal processing algorithms for noise suppression and signal decoupling.[11]

Two-dimensional transition metal dichalcogenides (2D TMDCs) such as tungsten disulfide (WS_2) offer exceptional promise for multimodal sensing due to their tunable bandgaps (1.3−2.1 eV) and high surface-to-volume ratios.[20,21] Heterostructures engineered by coupling TMDCs with metal oxides (e.g., titanium dioxide (TiO_2); E_g = 3.2 eV) enable precise modulation of charge transport dynamics via band alignment,

Received: March 26, 2025
Revised: June 1, 2025
Accepted: June 2, 2025

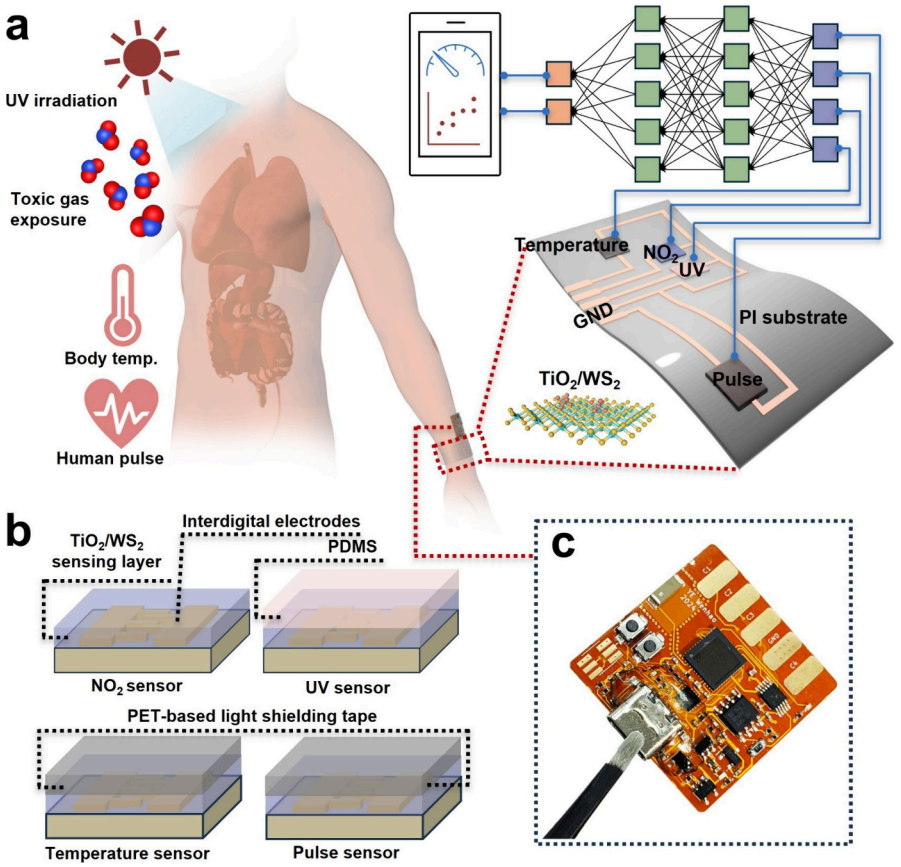

Figure 1. Schematic of the integrated wearable multimodal sensing system. (a) Functionality and architecture of the integrated wearable multimodal sensing system. (b) Device structure of NO_2, UV, temperature, and pulse sensors. (c) Photograph of the FPCB.

enhancing sensitivity and selectivity beyond pristine materials.[22,23] Herein, we present a wrist-worn multimodal sensing platform for the concurrent monitoring of environmental NO_2, UV irradiance, epidermal temperature, and human pulse signals (Figure 1). The system employs a TiO_2/WS_2 nanocomposite as a universal sensing material,[24,25] deposited via screen printing on a polyimide (PI) substrate with patterned copper (Cu) interdigitated electrodes (IDEs) for monolithic integration (Figure 1a). Selective parameter detection is achieved through optimized packaging. An unencapsulated architecture is used for direct NO_2 detection. Polydimethylsiloxane (PDMS) encapsulation is used for UV detection to eliminate gas cross-sensitivity.[26,27] Polyethylene terephthalate (PET)-based light shielding tape (transmittance of <5% at 300−700 nm) is utilized for temperature and pulse monitoring (Figure 1b). The system incorporates a flexible printed circuit board (FPCB) for sensor driving and data real-time telemetry (Figure 1c). As a result, the wearable sensing system is capable of detecting NO_2 at room temperature with a 12-month stability, and it can accurately measure UV intensity ranging from 0.024 to 1.68 mW/cm^2. Meanwhile, it exhibits excellent capabilities in pressure sensing (1 N, response of ∼12%, response time of 180 ms), which can be used for human pulse detection, and demonstrates a thermal sensitivity of 0.22%/°C. A hybrid neuroevolutionary algorithm (GA-BP, genetic algorithm-optimized backpropagation) decouples photo-gas interactions, achieving a <3.5% average relative error in NO_2 quantification under variable UV conditions (0−0.24 mW/cm^2). Processed data are transmitted via Bluetooth to a dedicated mobile application, providing real-time visualization of physiological and environmental parameters through an intuitive graphical user interface (GUI). This integrated system demonstrates potential for point-of-care diagnostics and longitudinal health monitoring, bridging the gap between environmental exposure assessment and personalized healthcare.[15−28]

Figure 2a presents the schematic architecture of the TiO_2/WS_2 heterostructure-based NO_2 sensor. The sensor configuration employs a mechanically compliant polyimide (PI) substrate,[29,30] enabling robust operation under flexural stress. A homogeneous TiO_2/WS_2 nanocomposite sensing layer deposited via screen printing demonstrated the optimal surface morphology. WT_1−WT_3 indicate 2, 5, and 7 wt % TiO_2, respectively. Figure 2b illustrates the cross-sectional configuration, highlighting the uniform coverage of WT_2 on the interdigitated Au electrodes with the PI substrate (Figure S1). Figure 2c exhibits the high-resolution transmission electron microscopy (HR-TEM) characterization of the WT_2 nanocomposite, revealing the distinct lattice fringes with interplanar spacings of 0.30 and 0.32 nm corresponding to the (004) crystallographic plane of WS_2 and the (110) plane of anatase TiO_2, respectively. These crystallographic parameters align well with the X-ray diffraction (XRD) patterns in Figure 2d and Figure S2, where characteristic peaks at 14.3° (WS_2 (002)) and 25.3° (TiO_2 (101)) confirm successful heterostructure formation.[22] Complementary X-ray photoelectron spectroscopy (XPS) analysis in Figure 2e and Figure S3 verifies elemental composition through deconvoluted peaks for the W 4f, S 2p, Ti 2p, and O 1s orbitals. The observed shifts in the binding energy of the S 2p and Ti 2p peaks before and after combining

https://doi.org/10.1021/acs.nanolett.5c01881
Nano Lett. XXXX, XXX, XXX−XXX

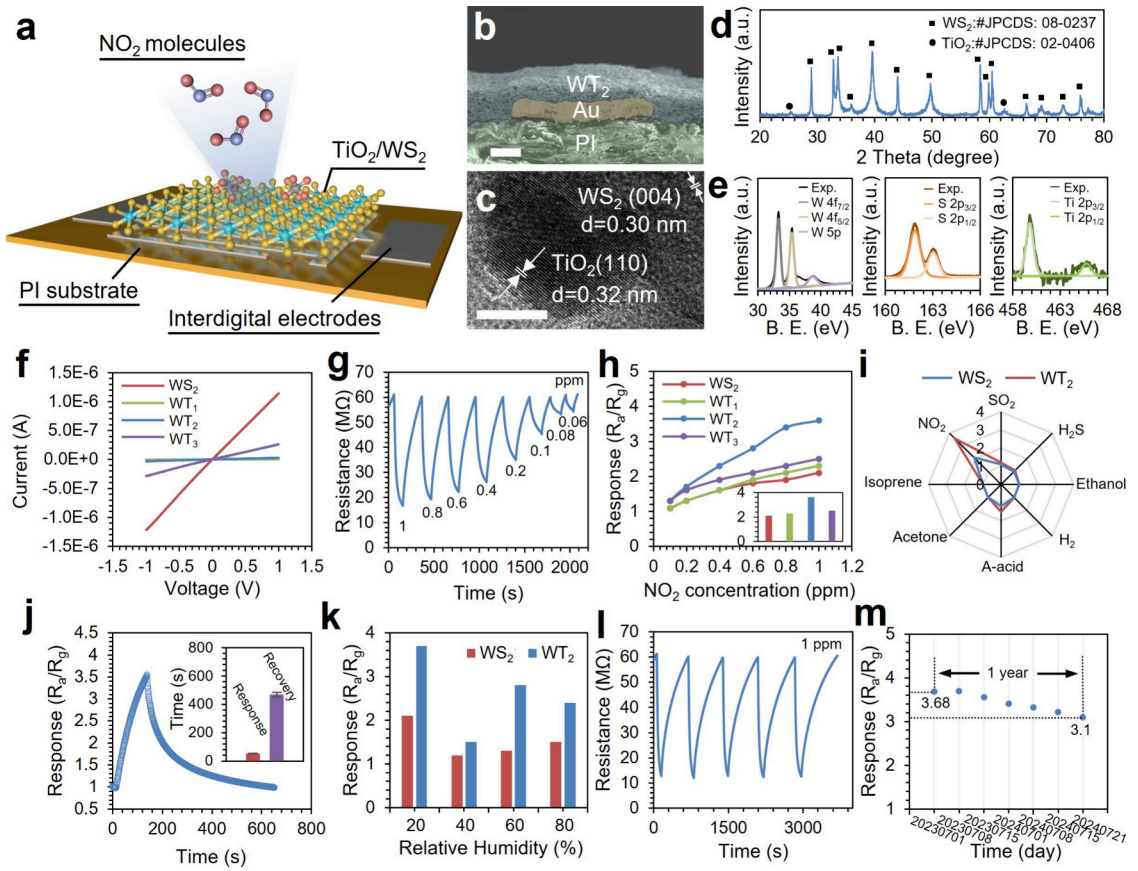

Figure 2. NO_2 sensor characterization. (a) Schematic illustration of the TiO_2/WS_2-based NO_2 sensor. (b) Scanning electron microscopy (SEM) image of the cross section of the sensor device. Scale bar, 20 μm. (c) HR-TEM image of the WT_2 sensing material. Scale bar, 10 nm. (d) XRD pattern of the WT_2 sensing material. (e) High-resolution XPS spectra of the W 4f, W 5p, S 2p, and Ti 2p orbitals of the WT_2 sensing material. (f) $I-V$ curves of WS_2-based sensors with different amounts of TiO_2. (g) Transient curve of WT_2 sensors vs NO_2 concentration. (h) Response vs NO_2 concentration curves of WS_2-based sensors with different amounts of TiO_2. The inset shows a histogram of the responses to 1 ppm NO_2. (i) Radar map showing a response comparison of the WS_2 and WT_2 sensors to different gases (1 ppm). (j) Plot of the response vs recovery time of WT_2 sensors to 1 ppm NO_2. (k) Histogram of the response comparison of WS_2 and WT_2 sensors to 1 ppm NO_2 with different relative humidities. (l) Transient curve of WT_2 sensors to 1 ppm NO_2 for five cycles. (m) Long-term stability of WT_2 sensors to 1 ppm NO_2.

WS_2 and TiO_2 (Figure S4) further confirm the formation of the heterojunction. TEM-energy dispersive spectroscopy (EDS) mapping confirms the homogeneous dispersion of constituent elements within the composite matrix (Figure S5).

Figure 2f delineates the current−voltage characteristics for TiO_2/WS_2 composites with varied ratios. The composite demonstrates a nonmonotonic resistance dependence on TiO_2 concentration, exhibiting an initial increase followed by a subsequent decrease. The initial increase in resistance arises from interfacial heterojunction formation between TiO_2 and WS_2,[31,32] which establishes energy band alignment and widens the depletion region, thereby impeding charge carrier mobility. At higher TiO_2 loadings (>5 wt %), a percolation threshold is surpassed, enabling the formation of interconnected TiO_2 conductive pathways that dominate charge transport, ultimately reducing the overall composite's resistivity.[33,34] Figure 2g and Figure S5 show the dynamic response profiles of WS_2 and WT_1-WT_3 sensors to different NO_2 concentrations. Response versus NO_2 concentration curves (Figure 2h) compare the sensing performance of WS_2-based sensors with different amounts of TiO_2, where the WT_2 composite demonstrates a substantial enhancement in its response ($Res._{1\ ppm}$ = 3.6) compared to pristine WS_2 ($Res._{1\ ppm}$ = 2.1) and TiO_2 ($Res._{1\ ppm}$ = 1.2 (Figure S7)). This performance improvement stems from band alignment modifications at the TiO_2/WS_2 interface, where charge transfer kinetics facilitate NO_2 chemisorption through molecular orbital hybridization.[35] The theoretical limit of detection (LOD) of the WT_2 sensor is calculated to be 14.4 ppb (Figure S8), which can meet the requirements of environmental NO_2 detection. Selectivity assessment in Figure 2i and Figure S9 reveals that the WT_2 sensor maintains excellent NO_2 discrimination against seven interfering gases (SO_2, H_2, H_2S, C_2H_2OH, a-acid, acetone, and isoprene) at equivalent concentrations (1 ppm). The transient response profile in Figure 2j quantifies the WT_2 sensor's response/recovery kinetics. An accelerated response (τ_{res} = 53 s) derives from heterojunction-enhanced charge separation efficiency (the WS_2 sensor's response time is 63 s, as shown in Figure S10). Relative humidity (RH) emerges as a critical operational parameter and indispensable environmental variable, governing gas sensor performance in real-world applications. As observed in Figure S11, the baseline resistance of WS_2 and WT_2 sensors increases as the relative humidity varies from 20% to 80%. The results reveal that as the relative humidity increases from 20% to 80%, the WT_2 sensor exhibits significantly reduced resistance variation compared to WS_2. This smaller drift in resistance under humid conditions suggests an enhanced moisture resistance in WT_2. Humidity-

https://doi.org/10.1021/acs.nanolett.5c01881
Nano Lett. XXXX, XXX, XXX−XXX

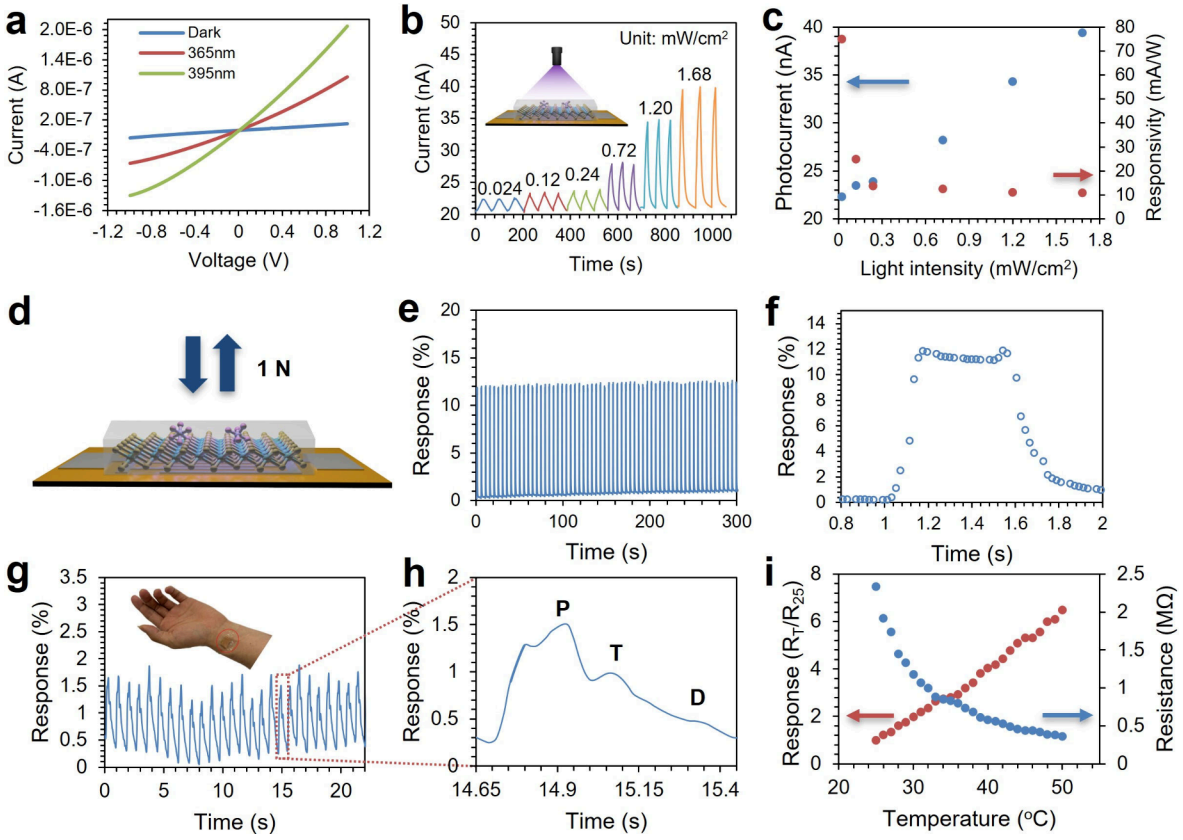

Figure 3. Performance characterization of UV, pressure (pulse), and temperature sensors. (a) $I-V$ curve of the UV sensor (dark, 365 and 395 nm light). (b) Time-domain photoresponse to different light intensities (395 nm). (c) Light intensity-dependent photocurrent and responsivity of the UV sensor. (d) Schematic of the pressure sensor with a 1 N pressure cycle test. (e) Transient curves of a piezoelectric sensor for a 1 N pressure cycle test. (f) Plot of the response vs recovery time of the pressure sensor. (g) Human pulse test diagram of the pressure sensor. (h) P, T, and D peaks of the pressure sensor under a single waveform in a pulse test. (i) Response and resistance of temperature sensors from 25 to 50 °C.

dependent performance analysis (Figure 2k and Figure S12) shows that both sensors suffer a decrease in their response at 40% RH due to competitive adsorption of water, while at high RH (60−80%), the composite leverages water's ionic properties to recover sensitivity. Repeatability evaluation (Figure 2i and Figure S13) demonstrates preserved cyclability across five cycles, while annual stability testing (Figure 2m and Figure S14) reveals a moderate performance decline (3.68 → 3.1 response to 1 ppm NO_2), maintaining practical viability for continuous environmental monitoring applications.[15−36]

The WT_2-based resistive UV sensor is encapsulated with PDMS to mitigate environmental interference from NO_2 and humidity. Figure 3a presents the $I-V$ characteristics of the UV sensor at 365 and 395 nm, as well as under dark conditions. The maximum I_{light}/I_{dark} values are 7.7 and 15.5 under a 0.5 V bias for 365 and 395 nm, respectively. Figure 3b shows the systematic investigation of the dependence of the photoresponse on irradiance intensity (0.024−1.68 mW/cm^2 at 395 nm), which reveals a linear correlation ($R^2 > 0.99$) between the photocurrent and incident light intensity, with the maximum responsivity reaching 75 mA/W at 0.024 mW/cm^2 (Figure 3c). For piezoresistive characterization, Figure 3d schematically illustrates the application of a 1 N normal force perpendicular to the WT_2 sensing matrix. Cyclic compression testing over 1200 cycles (Figure S15, partially shown in Figure 3e) demonstrates relatively good repeatability (standard deviation (SD) of 0.142, relative standard deviation (RSD) of 1.17%) with a consistent ∼12.07% response magnitude at 1 N loading, confirming robust mechanical durability. A single pulse (Figure 3f) extracted from Figure 3e indicates the rapid response stabilization (τ_{res} = 180 ms, τ_{rec} = 280 ms). Furthermore, Figure 3g presents real-time human pulse monitoring,[37] with Figure 3h resolving distinct P, T, and D peaks corresponding to systolic/diastolic events.[38] Temperature-dependent resistance analysis (Figure 3i) exhibits negative temperature coefficient (NTC) behavior (slope of response vs temperature α = 0.22%/°C) across the range of 25−50 °C, validating WT_2's multifunctionality and effectiveness. Meanwhile, the human body temperature (36−39 °C) causes negligible baseline drift in both NO_2 and UV sensors (Figure S16).

Figure 4a presents the response of the WT_2 sensor to NO_2 concentration (0.2−2 ppm) under UV illumination (395 nm, 0.024−0.24 mW/cm^2). The range represents realistic scenarios such as full sunlight exposure, partially cloudy skies, and heavily overcast environments, aligning closely with the intensity of natural environmental solar spectra. The sensor demonstrates irradiance-dependent signal amplification, exhibiting a linear correlation (R^2 = 0.98 at 200 ppb NO_2) between the response magnitude and optical power density (Figure 4b). Comparative analysis reveals a 155% enhancement in response at 0.24 mW/cm^2 relative to dark conditions. This synergistic enhancement arises from photoactivated mechanisms: (1) UV-induced electron−hole pair generation in TiO_2, modulating NO_2 adsorption/desorption kinetics, and (2) WS_2-mediated charge transfer amplification upon NO_2 chemisorption. To resolve the photo-gas interdependencies for precise NO_2

https://doi.org/10.1021/acs.nanolett.5c01881
Nano Lett. XXXX, XXX, XXX−XXX

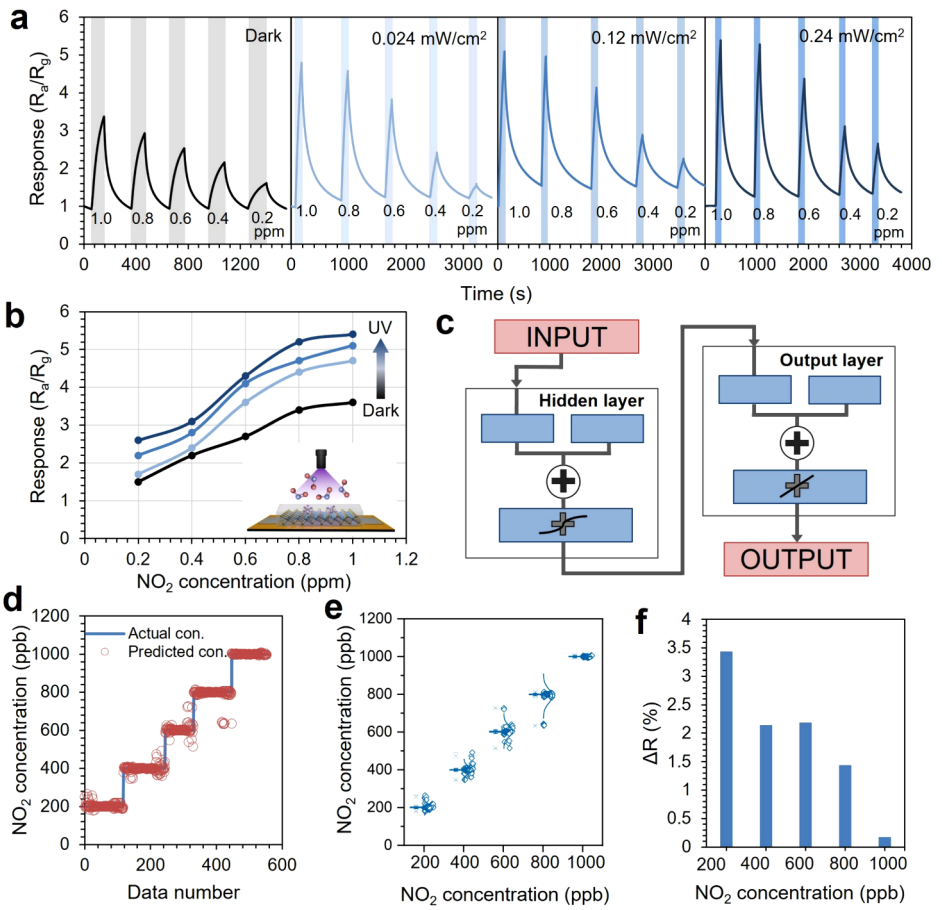

Figure 4. Effect of UV irradiation on NO_2 sensor performance and utilization of the GA-BP neural network for calibration. (a) Transient sensing curves of the WT_2 sensor to different concentrations of NO_2 under different light intensities of 395 nm UV irradiation. (b) Plot of the response vs NO_2 concentration under different light intensities of 395 nm UV irradiation. (c) Schematic diagram of the GA-BP neural network. (d) Predicted concentration by the GA-BP neural network. Data number refers to the number of data we used for algorithm processing. (e) Statistical distribution of predicted concentrations. (f) Average relative error between predicted concentrations and actual concentrations.

concentration quantification, we implement the GA-BP neural network architecture (Figure 4c). This framework addresses conventional BP NN limitations (convergence of local minima, hyperparameter sensitivity) through stochastic initialization, evolutionary optimization, and dynamic fitness evaluation,[39,40] making it a powerful tool for complex problem solving and data-driven decision making. Figure 4d validates the model's predictive accuracy across 532 test instances, achieving a maximum mean square error (MSE) of 3.36 ppb between experimental and predicted values (Figure 4e), demonstrating significant performance improvement over the standard BP model (Figure S19). Quantification accuracy is evaluated using the average relative error (ΔR) between the predicted concentration and the actual concentration:

$$\Delta R = \frac{\mathrm{Mean}(\mathrm{Abs}(\mathrm{Pre}_{gas} - \mathrm{Act}_{gas}))}{\mathrm{Act}_{gas}} \times 100\% \quad (1)$$

where Pre_{gas} and Act_{gas} represent the average of the predicted and actual NO_2 concentration, respectively. Figure 4f demonstrates the sub-parts per million resolution with $\Delta R <$ 3.43% at 200 ppb NO_2, decreasing to 0.17% at 1 ppm, which proves the reliability of our multimodal sensing system for NO_2 monitoring.

Figure 5a schematically depicts a wearable multimodal sensing system comprising an integrated sensor array patch and an FPCB on a human forearm. The sensor array patch employs anatomical optimization. NO_2, temperature, and UV sensors occupy the distal forearm positioning, while the piezoresistive pulse sensor is positioned over the radial artery for optimal arterial waveform detection. Figure 5b details the FPCB architecture, featuring five signal channels (R-NO_2, I-UV, R-temperature, R-pulse, and ground (GND)) with voltage dividers for sensor signal conditioning. The system implements four-channel multiplexed scanning with 16-bit analog-to-digital conversion (ADC). The microcontroller unit (MCU) orchestrates data packetization and power management.[41] Wireless connectivity via Bluetooth enables real-time telemetry to a dedicated Android application. Figure 5c showcases the heterogeneous sensor patch, where the WT_2 nanocomposite is screen-printed onto interdigitated Cu electrodes on PI substrates, achieving good adhesion stability under a 5 mm bending radius. As shown in Figure S20, we systematically compared the performance of Cu and Au electrode sensors to investigate the potential influence of the metal electrode−semiconductor contact. The results show essentially comparable performance between sensors with different electrode materials, indicating that signal changes primarily arise from the surface-sensing material layer. System integration (Figure 5d) demonstrates epidermal conformality with negligible motion artifacts during ambulatory testing. The GUI in Figure 5e visualizes time-synchronized data streams (UV index, body

https://doi.org/10.1021/acs.nanolett.5c01881
Nano Lett. XXXX, XXX, XXX−XXX

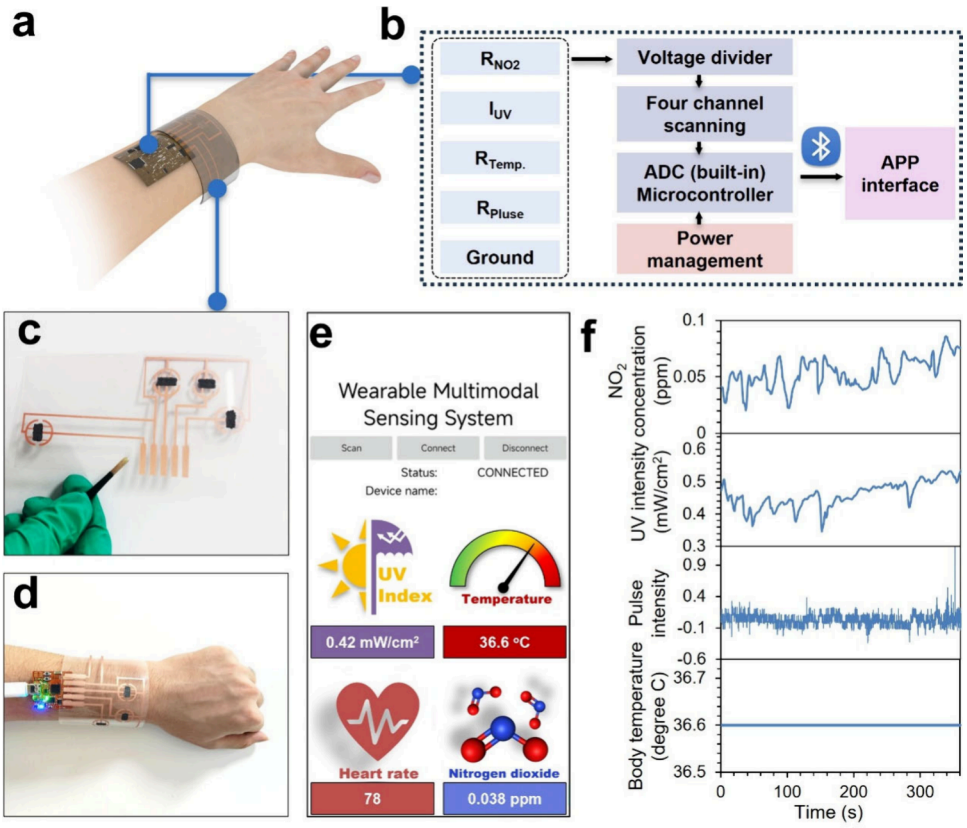

Figure 5. Continuous monitoring of the index using a wearable multimodal sensing system. (a) Schematic of the wearable multimodal sensing system with the integrated sensor patch and FPCB on a human arm. (b) Logic diagram of the circuit design. (c) Photo of the flexible integrated sensor patch. (d) Photo of the wearable multimodal sensing system in working mode. (e) App user interface. (f) Real-time recorded data using the wearable multimodal sensing system.

temperature, heart rate, and NO_2 concentration). Figure 5f presents ambulatory field-test data, demonstrating the immense potential of our multimodal sensing system in capturing the concurrent physiological baseline and environmental perturbations.

In summary, this work introduces a unified platform employing a TiO_2/WS_2 nanocomposite as a universal sensing material. The heterostructure leverages tunable bandgaps and high surface activity for enhanced NO_2 detection (response of 3.6 at 1 ppm) and UV sensing (75 mA/W responsivity at 0.024 mW/cm^2), while PDMS encapsulation and PET shielding mitigate environmental interference. The system concurrently monitors physiological parameters, demonstrating a 12% resistance change under a 1 N force for pulse detection and 0.22%/°C thermal sensitivity. A GA-BP neural network resolves photo-gas crosstalk, achieving a <3.5% error in NO_2 quantification under variable UV conditions. Integrated with an FPCB and Bluetooth-enabled GUI, the platform provides real-time visualization of NO_2, UV, temperature, and pulse data during ambulatory testing. This work establishes a scalable framework for multifunctional wearables, combining environmental exposure tracking with longitudinal health diagnostics.

■ ASSOCIATED CONTENT

Supporting Information

The Supporting Information is available free of charge at https://pubs.acs.org/doi/10.1021/acs.nanolett.5c01881.

Experimental method, SEM images, XRD profiles, XPS spectra, EDS mapping, NO_2 sensing properties, transient curves of the piezoelectric sensor, model optimization of the GA-BP neural network, regression analysis of the NO_2 concentration, comparison of the BP and GA-BP models, and comparison of sensing performance with Cu and Au electrodes (PDF)

■ AUTHOR INFORMATION

Corresponding Authors

Yongshun Liu − *State Key Laboratory of Integrated Optoelectronics (JLU Region), College of Electronic Science and Engineering, Jilin University, Changchun 130012, China*; Email: liuyongshun@jlu.edu.cn

Chen Wang − *State Key Laboratory of Integrated Optoelectronics (JLU Region), College of Electronic Science and Engineering, Jilin University, Changchun 130012, China*; orcid.org/0000-0002-5678-5287; Email: eechenw@jlu.edu.cn

Peng Sun − *State Key Laboratory of Integrated Optoelectronics (JLU Region), College of Electronic Science and Engineering and International Center of Future Science, Jilin University, Changchun 130012, China*; orcid.org/0000-0002-9509-9431; Email: pengsun@jlu.edu.cn

Authors

Qisong Jia − *State Key Laboratory of Integrated Optoelectronics (JLU Region), College of Electronic Science and Engineering, Jilin University, Changchun 130012, China*

https://doi.org/10.1021/acs.nanolett.5c01881
Nano Lett. XXXX, XXX, XXX−XXX

Wenhao Ye − *Department of Electronic and Computer Engineering, The Hong Kong University of Science and Technology, Kowloon, Hong Kong SAR 999077, China*
Chang Zhang − *State Key Laboratory of Integrated Optoelectronics (JLU Region), College of Electronic Science and Engineering, Jilin University, Changchun 130012, China*
Zhuoyi Jia − *State Key Laboratory of Integrated Optoelectronics (JLU Region), College of Electronic Science and Engineering, Jilin University, Changchun 130012, China*
Ji Liu − *State Key Laboratory of Integrated Optoelectronics (JLU Region), College of Electronic Science and Engineering, Jilin University, Changchun 130012, China*
Tongchao Wang − *State Key Laboratory of Integrated Optoelectronics (JLU Region), College of Electronic Science and Engineering, Jilin University, Changchun 130012, China*
Liupeng Zhao − *State Key Laboratory of Integrated Optoelectronics (JLU Region), College of Electronic Science and Engineering, Jilin University, Changchun 130012, China*
Zhiyong Fan − *Department of Electronic and Computer Engineering, The Hong Kong University of Science and Technology, Kowloon, Hong Kong SAR 999077, China;* orcid.org/0000-0002-5397-0129
Geyu Lu − *State Key Laboratory of Integrated Optoelectronics (JLU Region), College of Electronic Science and Engineering and International Center of Future Science, Jilin University, Changchun 130012, China*

Complete contact information is available at: https://pubs.acs.org/10.1021/acs.nanolett.5c01881

Author Contributions

Q.J. and W.Y. contributed equally to this work. C.W., P.S., and Q.J. conceived the idea and designed the experiments. C.W., Y.L., and P.S. supervised the research. Q.J., W.Y., and C.Z. carried out the synthesis experiment, material characterization, sensor fabrication, and sensor test. W.Y. designed the flexible PCB and App interface. Z.J. and J.L. helped with material characterization. L.Z. helped with data analysis. C.W., P.S., Q.J., W.Y., Z.F., and G.L. co-wrote the manuscript. All authors analyzed and discussed the results. All authors have given approval to the final version of the manuscript.

Notes

The authors declare no competing financial interest.

■ ACKNOWLEDGMENTS

The authors acknowledge the financial support received from the National Key Research and Development Program of China (2022YFB3205500) and the National Natural Science Foundation of China (62427805 and U23A20360).

■ ABBREVIATIONS

UV, ultraviolet; NO_2, nitrogen dioxide; 2D TMDCs, two-dimensional transition metal dichalcogenides; PI, polyimide; Cu, copper; IDEs, interdigitated electrodes; PDMS, polydimethylsiloxane; PET, polyethylene terephthalate; FPCB, flexible printed circuit board; GA-BP, genetic algorithm-optimized backpropagation; GUI, graphical user interface; HR-TEM, high-resolution transmission electron microscopy; SEM, scanning electron microscopy; XRD, X-ray diffraction; XPS, X-ray photoelectron spectroscopy; EDS, energy dispersive spectroscopy; *I*−*V*, current−voltage; LOD, limit of detection; RH, relative humidity; RSD, relative standard deviation; NTC, negative temperature coefficient; MSE, mean square error; ADC, analog-to-digital conversion; MCU, microcontroller; GND, Ground

■ REFERENCES

(1) Fang, H.; Ma, S.; Wang, J.; Zhao, L.; Nie, F.; Ma, X.; Lü, W.; Yan, S.; Zheng, L. Multimodal In-Sensor Computing Implemented by Easily-Fabricated Oxide-Heterojunction Optoelectronic Synapses. *Adv. Funct. Mater.* **2024**, *34* (49), No. 2409045.
(2) Gao, J.; Niu, H.; Li, Y.; Li, Y. Machine-Learning Enabled Biocompatible Capacitive-Electromyographic Bimodal Flexible Sensor for Facial Expression Recognition. *Adv. Funct. Mater.* **2025**, *35* (14), 18463.
(3) Dai, X.; Wu, Y.; Liang, Q.; Yang, J.; Huang, L. B.; Kong, J.; Hao, J. Soft Robotic-Adapted Multimodal Sensors Derived from Entirely Intrinsic Self-Healing and Stretchable Cross-Linked Networks. *Adv. Funct. Mater.* **2023**, *33* (44), No. 2304415.
(4) Hossain, M. M.; Lubna, M. M.; Bradford, P. D. Multifunctional and Washable Carbon Nanotube-Wrapped Textile Yarns for Wearable E-Textiles. *ACS Appl. Mater. Interfaces* **2023**, *15* (2), 3365−3376.
(5) He, Y.; Xu, X.; Xiao, S.; Wu, J.; Zhou, P.; Chen, L.; Liu, H. Research Progress and Application of Multimodal Flexible Sensors for Electronic Skin. *ACS Sens.* **2024**, *9* (5), 2275−2293.
(6) Liu, H.; Xiang, H.; Li, Z.; Meng, Q.; Li, P.; Ma, Y.; Zhou, H.; Huang, W. Flexible and Degradable Multimodal Sensor Fabricated by Transferring Laser-Induced Porous Carbon on Starch Film. *ACS Sustain. Chem. Eng.* **2020**, *8* (1), 527−533.
(7) Li, Z.; Li, Z.; Tang, W.; Yao, J.; Dou, Z.; Gong, J.; Li, Y.; Zhang, B.; Dong, Y.; Xia, J.; et al. Crossmodal sensory neurons based on high-performance flexible memristors for human-machine in-sensor computing system. *Nat. Commun.* **2024**, *15* (1), 7275.
(8) Luo, Y.; Li, J.; Ding, Q.; Wang, H.; Liu, C.; Wu, J. Functionalized Hydrogel-Based Wearable Gas and Humidity Sensors. *Nano-Micro Lett.* **2023**, *15* (1), 136.
(9) Tabatabaee, R. S.; Naghdi, T.; Peyravian, M.; Kiani, M. A.; Golmohammadi, H. An Invisible Dermal Nanotattoo-Based Smart Wearable Sensor for eDiagnostics of Jaundice. *ACS Nano* **2024**, *18* (41), 28012−28025.
(10) Wang, F.; Wang, S.; Liu, Y.; Ouyang, S.; Sun, D.; Yang, X.; Li, J.; Wu, Z.; Qian, J.; Zhao, Z.; Wang, L.; Jia, C.; Ma, S. Cellulose Nanofiber-Based Triboelectric Nanogenerators for Efficient Air Filtration in Harsh Environments. *Nano Lett.* **2024**, *24* (9), 2861−2869.
(11) Niu, G.; Wang, Z.; Xue, Y.; Yan, J.; Dutta, A.; Chen, X.; Wang, Y.; Liu, C.; Du, S.; Guo, L.; Zhou, P.; Cheng, H.; Yang, L. Pencil-on-Paper Humidity Sensor Treated with NaCl Solution for Health Monitoring and Skin Characterization. *Nano Lett.* **2023**, *23* (4), 1252−1260.
(12) Wang, X.; Qin, J.; Hu, Q.; Das, P.; Wen, P.; Zheng, S.; Zhou, F.; Feng, L.; Wu, Z. S. Multifunctional Mesoporous Polyaniline/Graphene Nanosheets for Flexible Planar Integrated Microsystem of Zinc Ion Microbattery and Gas Sensor. *Small* **2022**, *18* (29), No. e2200678.
(13) Won, S. M.; Wang, H.; Kim, B. H.; Lee, K.; Jang, H.; Kwon, K.; Han, M.; Crawford, K. E.; Li, H.; Lee, Y.; Yuan, X.; Kim, S. B.; Oh, Y. S.; Jang, W. J.; Lee, J. Y.; Han, S.; Kim, J.; Wang, X.; Xie, Z.; Zhang, Y.; Huang, Y.; Rogers, J. A. Multimodal Sensing with a Three-Dimensional Piezoresistive Structure. *ACS Nano* **2019**, *13* (10), 10972−10979.
(14) Lu, Y.; Xu, K.; Zhang, L.; Deguchi, M.; Shishido, H.; Arie, T.; Pan, R.; Hayashi, A.; Shen, L.; Akita, S.; Takei, K. Multimodal Plant Healthcare Flexible Sensor System. *ACS Nano* **2020**, *14* (9), 10966−10975.
(15) Xu, F.; Li, X.; Shi, Y.; Li, L.; Wang, W.; He, L.; Liu, R. Recent Developments for Flexible Pressure Sensors: A Review. *Micromachines* **2018**, *9* (11), 580.
(16) Yan, C.; Li, X.; Wang, X.; Liu, G.; Yang, Z.; Tian, H.; Wang, C.; Chen, X.; Shao, J. Extremely Stable, Multidirectional, All-in-One Piezoelectric Bending Sensor with Cycle up to Million Level. *Adv. Funct. Mater.* **2024**, *34* (49), No. 2409093.

(17) Kang, T. W.; Lee, Y. J.; Rigo, B.; Soltis, I.; Lee, J.; Kim, H.; Wang, G.; Zavanelli, N.; Ayesh, E.; Sohail, W.; Majditehran, H.; Kozin, S. H.; Hammond, F. L., III; Yeo, W. Soft Nanomembrane Sensor-Enabled Wearable Multimodal Sensing and Feedback System for Upper-Limb Sensory Impairment Assistance. *ACS Nano* **2025**, *19* (5), 5613−5628.
(18) Liu, H.; Xiang, H.; Wang, Y.; Li, Z.; Qian, L.; Li, P.; Ma, Y.; Zhou, H.; Huang, W. A Flexible Multimodal Sensor That Detects Strain, Humidity, Temperature, and Pressure with Carbon Black and Reduced Graphene Oxide Hierarchical Composite on Paper. *ACS Appl. Mater. Interfaces* **2019**, *11* (43), 40613−40619.
(19) Ma, X.; Wang, C.; Wei, R.; He, J.; Li, J.; Liu, X.; Huang, F.; Ge, S.; Tao, J.; Yuan, Z.; et al. Bimodal Tactile Sensor without Signal Fusion for User-Interactive Applications. *ACS Nano* **2022**, *16* (2), 2789−2797.
(20) Lee, E.; Yoon, Y. S.; Kim, D. J. Two-Dimensional Transition Metal Dichalcogenides and Metal Oxide Hybrids for Gas Sensing. *ACS Sens.* **2018**, *3* (10), 2045−2060.
(21) Kim, Y.; Kwon, K. C.; Kang, S.; Kim, C.; Kim, T. H.; Hong, S. P.; Park, S. Y.; Suh, J. M.; Choi, M. J.; Han, S.; Jang, H. W. Two-Dimensional NbS_2 Gas Sensors for Selective and Reversible NO_2 Detection at Room Temperature. *ACS Sens.* **2019**, *4* (9), 2395−2402.
(22) Lu, Z.; Cao, Z.; Hu, E.; Hu, K.; Hu, X. Preparation and tribological properties of WS2 and WS_2/TiO_2 nanoparticles. *Tribol. Int.* **2019**, *130*, 308−316.
(23) Singh, A. K.; Walia, R.; Chauhan, M. S.; Singh, R. S.; Singh, V. K. Performance analysis of n-TiO_2/p-Cu_2O, n-TiO_2/p-WS_2/p-Cu_2O, and n-TiO_2/p-WS_2 heterojunction solar cells through numerical modelling. *Environ. Sci. Pollut. Res.* **2023**, *30*, 98718−98731.
(24) Nada, E. A.; El-Maghrabi, H. H.; Raynaud, P.; Ali, H. R.; Abd El-Wahab, S.; Sabry, D. Y.; Moustafa, Y. M.; Nada, A. A. Enhanced Photocatalytic Activity of WS_2/TiO_2 Nanofibers for Degradation of Phenol under Visible Light Irradiation. *Inorganics* **2022**, *10* (4), 54.
(25) Gu, G. Y.; Shang, J.; Zhang, X. Y. Improved frictional properties of WS_2/TiO_2 composite layer in situ prepared on TC4 alloy. *Chalcogenide Lett.* **2022**, *19* (12), 955−964.
(26) Amjadi, A.; Hosseini, M. S.; Ashjari, T.; Roghabadi, F. A.; Ahmadi, V.; Jalili, K. Durable Perovskite UV Sensor Based on Engineered Size-Tunable Polydimethylsiloxane Microparticles Using a Facile Capillary Microfluidic Device from a High-Viscosity Precursor. *ACS Omega* **2020**, *5* (2), 1052−1061.
(27) Zimmermann, C. A.; Amouzou, K. N.; Sengupta, D.; Kumar, A.; Demarquette, N. R.; Ung, B. Novel elastomeric spiropyran-doped poly(dimethylsiloxane) optical waveguide for UV sensing. *Front. Optoelectron.* **2024**, *17* (1), 21.
(28) Zhou, K.; Ding, R.; Ye, W.; Huang, J.; Zhou, Z.; Huang, L.; Ma, X.; Fan, Z.; Lin, Y. A Fully Printable and Integrated System with Long-Term Stability for Versatile and Multimodal Perspiration Tracking. *Nano Lett.* **2024**, *24* (47), 15092−15100.
(29) Yang, C.; Wang, H.; Zhou, G.; Zhao, H.; Hou, W.; Zhu, S.; Zhao, Y.; Sun, B. A Multimodal Perception-Enabled Flexible Memristor with Combined Sensing-Storage-Memory Functions for Enhanced Artificial Injury Recognition. *Small* **2024**, *20* (45), No. e2402588.
(30) Zhang, C.; Chen, J.; Gao, J.; Tan, G.; Bai, S.; Weng, K.; Chen, H. M.; Ding, X.; Cheng, H.; Yang, Y.; et al. Laser Processing of Crumpled Porous Graphene/MXene Nanocomposites for a Stand-alone Gas Sensing System. *Nano Lett.* **2023**, *23* (8), 3435−3443.
(31) Yang, X.; Yang, Q.; Wang, X.; Li, J.; Fu, Q.; Wang, W.; Zhang, R.; Li, Y.; Chen, L.; Cao, J.; Zhang, Y. Micro-mechanism Study of Charge Transfer at Heterojunction Interface Based on First-Principles Theory: MoS_2/SnO_2 as the Prototype. *Chem. Phys. Lett.* **2024**, *856*, No. 141639.
(32) Jia, Y.; Zhang, Z.; Xiao, L.; Lv, R. Carbon Nanotube-Silicon Nanowire Heterojunction Solar Cells with Gas-Dependent Photovoltaic Performances and Their Application in Self-Powered NO_2 Detecting. *Nanoscale Res. Lett.* **2016**, *11* (1), 299.
(33) Chen, Y.; Wu, J.; Xu, Z.; Shen, W.; Wu, Y.; Corriou, J.-P. Computational Assisted Tuning of Co-doped TiO_2 Nanoparticles for Ammonia Detection at Room Temperatures. *Appl. Surf. Sci.* **2022**, *601*, No. 154214.
(34) Lee, J.-H.; Mirzaei, A.; Kim, J.-H.; Kim, J.-Y.; Nasriddinov, A. F.; Rumyantseva, M. N.; Kim, H. W.; Kim, S. S. Gas-sensing Behaviors of TiO_2-layer-modified SnO_2 Quantum Dots in Self-heating Mode and Effects of the TiO_2 Layer. *Sens. Actuators B: Chem.* **2020**, *310*, No. 127870.
(35) Liu, H.; Zhang, W.; Yu, H.; Gao, L.; Song, Z.; Xu, S.; Li, M.; Wang, Y.; Song, H.; Tang, J. Solution-Processed Gas Sensors Employing SnO_2 Quantum Dot/MWCNT Nanocomposites. *ACS Appl. Mater. Interfaces* **2016**, *8* (1), 840−846.
(36) Xiong, J.; Cai, Y.; Nie, X.; Wang, Y.; Song, H.; Sharif, H. M. A.; Li, Z.; Li, C. PANI/3D Crumpled Ti_3C_2TX/TiO_2 Nanocomposites for Flexible Conductometric NH_3 Sensors Working at Room Temperature. *Sens. Actuators B: Chem.* **2023**, *390*, No. 133987.
(37) Yang, T.; Jiang, X.; Zhong, Y.; Zhao, X.; Lin, S.; Li, J.; Li, X.; Xu, J.; Li, Z.; Zhu, H. A Wearable and Highly Sensitive Graphene Strain Sensor for Precise Home-Based Pulse Wave Monitoring. *ACS Sens.* **2017**, *2* (7), 967−974.
(38) Park, D. Y.; Joe, D. J.; Kim, D. H.; Park, H.; Han, J. H.; Jeong, C. K.; Park, H.; Park, J. G.; Joung, B.; Lee, K. J. Self-Powered Real-Time Arterial Pulse Monitoring Using Ultrathin Epidermal Piezoelectric Sensors. *Adv. Mater.* **2017**, *29* (37), No. 1702308.
(39) Zhang, J.; Hu, C.; Yan, H. A DPSO-BP NN Modeling for Predicting Mechanical Property: A Case of 6181H18 Aluminum Alloy. *Appl. Phys. A: Mater. Sci. Process.* **2024**, *130* (4), 257.
(40) Gao, Z.; Jin, L.; Liu, P.; Wei, J. Height Prediction of Water-Conducting Fracture Zone in Jurassic Coalfield of Ordos Basin Based on Improved Radial Movement Optimization Algorithm Back-Propagation Neural Network. *Mathematics* **2024**, *12* (10), 1602.
(41) Wang, J.; Yan, K.; Li, X.; Zong, Y.; Xu, Q.; Sun, X. Hollow Polyaniline Microspheres Decorated Fabric Sensor with Electromagnetic Wave-Absorbing and Multimodal Sensing Toward Human−Machine Interaction. *Adv. Funct. Mater.* **2025**, *35* (13), No. 24018071.

https://doi.org/10.1021/acs.nanolett.5c01881
Nano Lett. XXXX, XXX, XXX−XXX